Article

Synchrotron-Based X-ray Photoelectron Microscopy of LMO/LAGP/Cu Thin-Film Solid-State Lithium Metal Batteries

Majid Kazemian [1], Matteo Amati [2], Luca Gregoratti [2], Maya Kiskinova [2] and Benedetto Bozzini [3,*

[1] Diamond Light Source Ltd., Harwell Science and Innovation Campus, Didcot, Oxfordshire OX11 0DE, UK; majid.kazemian@diamond.ac.uk
[2] Elettra—Sinctrotrone Trieste S.C.p.A. S.S 14, km 163.5 in Area Science Park, 34149 Trieste-Basovizza, Italy; matteo.amati@elettra.eu (M.A.); luca.gregoratti@elettra.eu (L.G.); maya.kiskinova@elettra.eu (M.K.)
[3] Department of Energy, Politecnico di Milano, Via Lambruschini 4, 20156 Milano, Italy
* Correspondence: benedetto.bozzini@polimi.it

Abstract: Solid-state batteries (SSB), characterized by solid-state electrolytes—in particular inorganic ones (ISSE)—are an ideal option for the safe implementation of metallic Li anodes. Even though SSBs with ISSEs have been extensively investigated over the last two decades, they still exhibit a series of technological drawbacks. In fact, mechano-chemical issues, mainly the stability of the electrolyte/anode interface, hinder their widespread application. The present investigation focusses on a thin-film LMO (Lithium-Manganese-Oxide)/LAGP (LiAlGe Phosphate)/Copper, anodeless Lithium-metal battery and explores the morphochemical evolution of the electrode/electrolyte interfaces with synchrotron-based Scanning Photoelectron Microscopy (SPEM) of intact pristine and cycled cells. Chemical images were acquired with submicrometer resolution, to highlight the coupled geometrical and chemical-state changes caused by electrochemical ageing. Geometrical changes of the electrolyte/cathode interface were induced by periodic volume changes, causing de-cohesion of the solid-solid contact, but no chemical-state changes accompany the cathodic damaging mode. Instead, shape changes of the electrolyte/anode region pinpoint the correlation between mechanical damaging with the decomposition of the LAGP ISSE, due to the reduction of Ge, triggered by the contact with elemental Li. The micro-spectroscopic approach adopted in this study enabled the assessment of the highly localized nature of the cathodic and anodic degradation modes in SSB devices and to single out the chemical and mechanical contributions.

Keywords: solid-state batteries; solid electrolyte; spectromicroscopy; SPEM; XPS; LAGP

1. Introduction

Combining the high energy density allowed by metallic Li with safety and durability is a key challenge for next-generation battery technologies. The solid-state battery (SSB) concept is a promising approach and the choice of inorganic solid-sate electrolytes (ISSE) instead of ionomers in principle can enable the best chemical and geometrical stability. In fact, ISSEs are inflammable, and their high stiffness can counteract Li outgrowth issues, since they exhibit typical single-crystal shear moduli that are ca. a factor of two higher than that of Li [1].

Moreover, the use of ISSEs opens up the microfabrication route for thin-film SSBs (TFSSB), which can be integrated with electronic devices [2]. Unfortunately, these desirable properties of ISSEs are counterbalanced by criticalities due to the degradation of solid electrolyte-electrode interfaces. In fact, cyclic volume changes of materials with different expansion coefficients, combined with decomposition processes triggered by the coupling of redox-active materials, can impair both the electrical contact between the two phases and the ionic conductivity of the electrolyte. Sometimes, in order to mitigate these issues, ionically conducting ceramics are combined with polymers or ionic liquids to form composite electrolytes. However, this would reduce the safety level of pure ISSEs and, possibly,

introduce other degradation modes. ISSE fabrication and electrochemical testing has been the object of intensive research, essentially over the last two decades, and has been summarized in a series of reviews [3–5]. ISSEs can be grouped into three classes: (i) oxide-based, (ii) sulphide-based, and (iii) phosphate-based. In this study, we have considered a system belonging to the last class: NASICON-type LAGP $Li_{1+x}Al_xGe_{2-x}(PO_4)_3$ [6–8]. Our choice has been guided by the functional properties, detailed below in Section 2.1. NASICON-type ceramics are characterized by the general formula $AM_2(PO_4)_3$, where A is a monovalent alkaline ion and M is a tetravalent transition metal ion. Structurally, these materials consist of a $M_2P_3O_{12}$ framework, with two MO_6 octahedra and three PO_4 tetrahedra, connected by corner-sharing O atoms. Alkali ions occupy interstitial positions, and can diffuse through the channel established by the array of MO_6 octahedra and PO_4 tetrahedra. In addition, the particular arrangement of metal-oxygen polyhedra of NASICON structures minimizes the electronic conductivity, yielding optimal electrolyte behaviour. Moreover, NASICON compounds can be ionically doped, allowing for structural tuning.

A variety of NASICON-type ISSEs has been studied, mainly based on $LiTi_2(PO_4)_3$ and $LiGe_2(PO_4)_3$ lattices, modified in two main ways: (i) partial substitution of tetravalent ions (Ti, Ge) with trivalent ones (Al, Ga, Fe) [9], and (ii) different types of doping, to modulate the crystal structure [10], in particular to form amorphous structures, whereby ionic conductivity is enhanced by suppressing the diffusion barriers at the grain boundaries [11]. The relatively high Li^+ conductivity of these materials is due to the combination of two factors: (i) the super-stoichiometry of this alkaline ion and (ii) the presence of tunnel structures exhibiting locally higher diffusion coefficients, due to atomic radius effects. Classical NASICON compounds are LAGP $Li_{1+x}Al_xGe_{2-x}(PO_4)_3$ and LATP $Li_{1.3}Al_{0.3}Ti_{1.7}(PO_4)_3$ and the former material is considered in the present investigation.

As stated above, degradation—mainly chemical, electrochemical, and mechanical—is a critical issue of ISSEs, including the NASICON-type ones. The better-known damaging modes of NASICON materials are listed below. (i) Reactive NASICON/Li contact, whereby LAGP and LATP yield Li-Ti-Ge alloys, as assessed by ex-situ SEM and XPS [12,13]. This chemical instability is favoured by electrochemical recharge conditions, leading to the reduction of Ti^{4+} and Ge^{4+} [14]: reductive degradation also leads to the formation of mixed electronically-ionically conducting (MEIC) layers [15], causing self-enhancing degradation. (ii) Reactive NASICON/cathode contact, leading to Li_3PO_4 formation (LAGP/LMN [16], LATP/LCO, LMO, LPF [17]). (iii) Mechanical stability, due to fabrication- and cycling-induced crystalline imperfections [18] and cracking [19], practically limits the dendrite suppression capability [20–23]. (iv) Furthermore, thermal stability issues have to be considered. Even though NASICON materials are intrinsically free from thermal runaway problems, their combination with Li (see, e.g., Ref. [24] for LAGP), but also with cathode compounds [17], can bring about exothermal reactions. The application of different types of layers at the NASICON/anode interface has been proposed to mitigate degradation: Ge [25]; Al_2O_3 [26]; $LiZr_2(PO)_4$ (decomposing in-situ to yield a stable, ionically conducting Li_3P/Li_8ZrO_6 composite) [27]; $Zn@Li_2O$ core-shell particles [28]; LiF/Li_3N [29].

This complex degradation scenario, often faced with trial-and-error fabrication approaches, calls for better physico-chemical insight. In particular, a close-knit group of in situ studies have appeared, addressing the following aspects. (i) XPS and AES studies of ISSE reactivity in contact with Li (LiPON [15,30,31], $Li_7P_3S_{11}$ [32], $Li_2S–P_2S_5$ [33]) and cathodic materials (Li_6PS_5Cl/LCO, NMC, and LMO [34]). (ii) Neutron depth profiling was employed to follow the anodic interphases of garnet [35], LiPON, LLZO, and amorphous Li_3PS_4 [22]. (iii) Electron holography was used to observe Li^+ shuttling in $Li_{1+x+y}Al_yTi_{2-y}Si_xP_{3-x}O_{12}$ [36] and to observe the electric potential distribution developing upon cycling [37]. (iv) Finally, the authors of this paper have recently employed soft-X ray based Near-Edge X-ray Absorption Fine Structure (NEXAFS) microspectroscopy to follow the modifications of the LAGP/Li interface, resulting from battery cycling [38]. In the present work, we demonstrate the possibility of using Scanning Photoelectron Microscopy (SPEM) to map the elemental and chemical-state distribution of the cathodic and

anodic interfaces with submicrometric precision. In this first study, chiefly addressing methodological aspects, we developed fabrication and time-lapse in-situ measurement protocols to analyse intact, full LAGP-based thin-film batteries in pristine condition and after prolonged cycling. Exactly the same devices and approach can be adopted for subsequent in operando studies.

2. Experimental

2.1. Microfabrication of the SSB

This SPEM study is centred on a microfabricated thin-film solid state battery, with LAGP ISSE, LMO cathode, and Li metal anode, plated onto a Cu current collector during the formation and recharge processes. This device exhibits the dual nature of being a concrete device for battery-integrated microelectronics and of being directly measurable with UHV-based methods, such as SPEM. The TFSSB structure includes structural support, cathodic and anodic current collectors, cathode, solid electrolyte, anode, and a capping layer that insulates Li, from the ambient.

LAGP (NASICON-type $Li_{1.5}Al_{0.5}Ge_{1.5}(PO_4)_3$) was selected for three main reasons: the stability of NASICON-type materials with respect to oxygen and humidity [39–41] and the wide electrochemical window (3.0–4.6 V, measured for a LMO/LAGP/Li TFSSB [42]). Moreover, NASICON-type films can be produced by PVD (Magneton-Sputtering) [43]. Regarding the anode, our TFSSN was fabricated in an anodeless configuration [44,45] with a current collector made of Cu that does not alloy with Li, onto which Li is electrodeposited during charging periods. LMO (Mn-based spinel-type $LiMn_2O_4$) was selected as the cathode material because it is environmentally stable and its implementation in thin-film form is well documented for SSBs [46]. Thin-film LMO cathodes can be grown by PVD (magnetron sputtering [47] and PLD [48]) and Plasma-enhanced CVD [49].

The cell configuration we adopted exhibits the electrode–electrolyte system in planar configuration, to optimize the imaging capability of electrode–electrolyte interfacial processes (Figure 1). The patterned electrodes and electrolyte were microfabricated with a four-step optical lithography and lift-off protocol at the PoliFab Facility of Politecnico di Milano, on commercial supported Si_3N_4 membranes (Si support: square, side 5.0 mm; Si_3N_4 membrane: square, side 0.5 mm, thickness 75 nm) supplied by Silson Ltd., Southam, UK. The current feeders were Au (cathodic, 30 nm) and Cu (anodic, 50 nm) films, deposited on 10 nm thick Cr adhesion layers. Au current collectors were successfully employed for TFSSB [50]. Cr and Au were sputtered (Z400 Leybold GmbH) and Cu was electron-beam evaporated (BAK 640 evaporator, Evatec AG). LMO (Merck) was also evaporated with a deposition rate of 0.2 nm/s, which ensures the growth of a nanocrystalline thin layers with optimal cycling properties in the potential interval 4.5 ÷ 3.0 V at ambient temperature [51]. The lift-off step for LMO was performed with an ethanol amine stripper. LMO was not heat-treated, as is customary for SSBs with bulk electrodes [52], to avoid chemical interaction with LAGP [53]. The LAGP electrolyte was RF sputtered, with the same system used for Cr and Au, to a thickness of 0.1 μm. To ensure the correct P/Ge ratio, we followed the protocol of Ref. [54]. We operated a nominally $Li_{1.5}Al_{0.5}Ge_{1.5}P_3O_{12}$ target (MSE PRO, our EDX target analysis: Ge 8.8 at%, Al 3 at%, P 17.6 at%, O 71 at%) in 4×10^{-2} mbar Ar in planar geometry, with a power density of 1.7 W cm^{-2}, substrate-to-target distance of 40 mm and growth rate of 5 nm min^{-1} [6]. Lift off was carried out with acetone. The LAGP electrolyte layer covered the whole device, also acting as a capping layer. This geometrical arrangement of the electrodes and electrolyte is appropriate for transmission experiments, such as spectro-STXM [38]. However, for the present SPEM study, aimed at following chemical variations of LAGP, the progress of the electrolyte reaction occurring at the electrode/electrolyte interfaces would yield a chemical front that propagates through the thickness of the electrolyte, emerging to the surface. Finally, the microfabricated devices were wire bonded on an IC socket adapter (Figure 1D). Figure 2 shows the functional part of the TFSSB and reports a selection of material characterizations. Figure 2A reports the EDX map of the cell: the electrochemically active region is the one capped with the

LAGP film (green area). As indicated above, for fabrication reasons, the cathode (blue) and anode (red) patches extend beyond the actual cell. The SEM micrographs of the LMO and LAGP layers (Figure 2B, Figure 2C$_1$, and Figure 2C$_2$, respectively)) show a homogeneous morphology micro-crystallite pattern. EDX spectra and quantitative analyses (Figure 2D,E) confirm that the nominal stoichiometry is preserved. X-ray diffractography (Figure 2F) and Raman spectroscopy (Figure 2G) prove that the correct crystal structures are obtained.
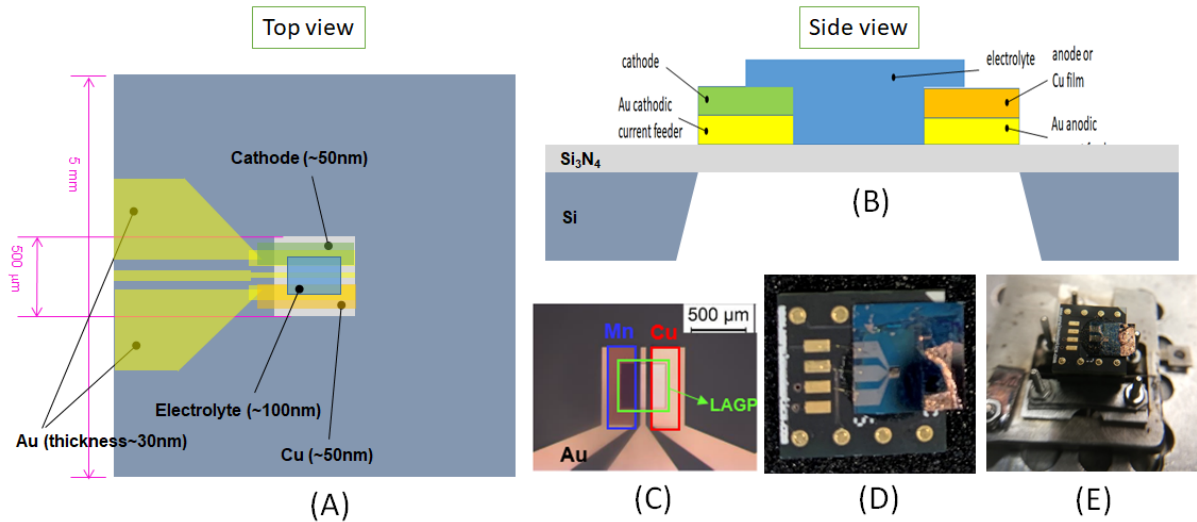

Figure 1. (**A**,**B**) The design of LMO/LAGP/Cu Li metal TFSSB. (**C**,**D**) Light microscope images of the microfabricated battery. (**E**) Battery mounted on the SPEM sample stage.
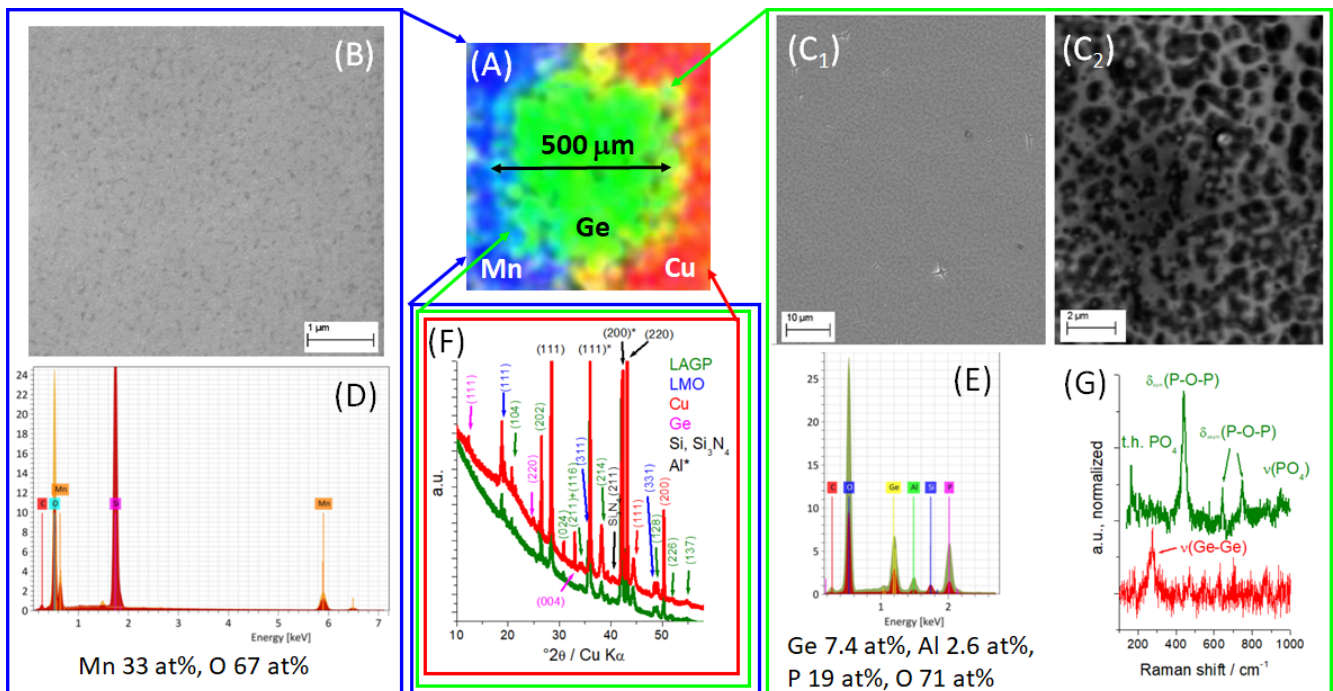

Figure 2. (**A**) EDX map of the pristine LMO/LAGP/Cu Li metal TFSSB, for: Mn (LMO cathode), Cu (anode) and Ge (LAGP electrolyte). SEM micrographs of LMO (**B**) and LAGP (**C$_1$**,**C$_2$**). (**D**,**E**) EDX spectra of LMO and LAGP. (**F**) X-ray diffractograms of pristine (green) and cycled (red) cell. (**G**) Raman spectra of pristine (green) and cycled (red) cell. Partly adapted from Ref. [38], with permission.

The X-ray diffractogram of Figure 2F, the green plot, shows reflections from the Cu (PDF 003-1018) anode support, the LMO (PDF 35-0782) cathode, and the LAGP electrolyte,

witnessing growth of well-crystallized LMO [55] and LAGP [8,56–59]. In addition, owing to the lack of lateral resolution of this measurement, peaks from the Si [60] and Si_3N_4 substrates [61] and the Al clips (PDF 85-1327) were also recorded.

The Raman spectrum, measured with a laser wavelength of 532 nm, exhibits a strong fluorescence, which can be reduced by appropriate filtering, at the cost of a low signal-to-noise ratio, which is sufficient for material characterization. The background- and cosmic rays corrected spectrum of Figure 2G, the green plot, shows the characteristic NASICON-type bands, coherently with literature data [57,59], dominated by the vibrational modes of PO_4 [62–64]. The key Raman spectral features are: t.h. PO_4, more translation-libration of phosphate tetrahedra; δ_{sym}(P-O-P) and δ_{asym}(P-O-P) symmetrical and antisymmetrical P-O-P bending and $\nu(PO_4)$ tetrahedron stretching.

2.2. Scanning PhotoElectron Microscopy (SPEM)

The SPEM measurements were carried out at Elettra synchrotron located in Trieste, Italy, using the ESCA Microscopy beamline. The incident monochromatic X-ray radiation is focused by means of zone plates (ZP) and demagnified to a submicrometer (down to 100 nm) spot onto the sample, which is raster scanning over the ZP focal plane perpendicular to the microprobe [65]. For each point during the scan, photoelectrones are collected with a SPECS-PHOIBOS 100 hemispherical analyzer to acquire spatially resolved photoemission spectra and chemical maps. The SPEM data for this work have been recorded with 0.2 eV energy resolution by using an incident beam of 650 eV photon energy.

3. Results and Discussion

The anodeless TFSSB was initially subjected to a formation step, consisting in de-intercalating Li^+ from the cathode and plating metallic Li onto the Cu current collector film, and subsequently cycled with the protocol, described in Section 3.1. The same TFSSBs in pristine and cycled conditions were studied by spectral STXM in [38]. The present SPEM-based study shows the feasibility of time-lapse in situ photoelectron studies of full devices and provides complementary electrochemical materials-science information.

3.1. Electrochemical Ageing

Our LAGP-capped TFSSBs, in a discharged state, are stable in humid air and can be freely moved from the glove-box, where they were electrochemically cycled, to the SPEM end-station. For the present investigation, five potentiostatic cycles between 4.5 and 3.0 V of 24 h each were used, terminating in the discharged state. Prolonged cycling of LMO/LiPON/Li TFSSBs was demostrated in this potential range [66]. Moreover, limiting the potential to 4.5 V was proved not only to nominally exclude parasitic reactions, but also to avoid changes in the lattice structure [51]. This electrochemical polarization program led to the attainment of vanishing current densities at the end of each charge/discharge cycle. Cycling was carried out in an Ar-filled glovebox, with an SP 50e Bio-logic potentiostat. The battery capacity and the cathode utilization degree, i.e., the fraction of cathodic material built in the SSB that is actually utilized for successive recharging processes [67], were evaluated by integrating the relaxing part of the chronoamperometric time-series (Figure 3). Figure 3A shows that ca. 50% of the initial specific nominal capacity corresponding to the formation at 4.5 V is lost after the first discharge at 3.0 V. It should be mentioned that this first-cycle loss is ca. a factor of 6 higher than that of TFSSBs designed for performance [47]. The suboptimal functional behaviour of our device dedicated for multimodal in situ studies, including transmission experiments, is acceptable for the current methodological purpose and can be improved, especially for surface-sensitive photon-in electron-out SPEM. After cycling, the structure of LAGP, as assessed by XRD and Raman, resulted to be modified. XRD (Figure 2F, red plot) shows the formation of a fraction of crystalline Ge [68]. The Raman spectrum is dominated by the characteristic Ge-Ge stretching mode of elemental Ge at ca. 275 cm^{-1} [69–71].
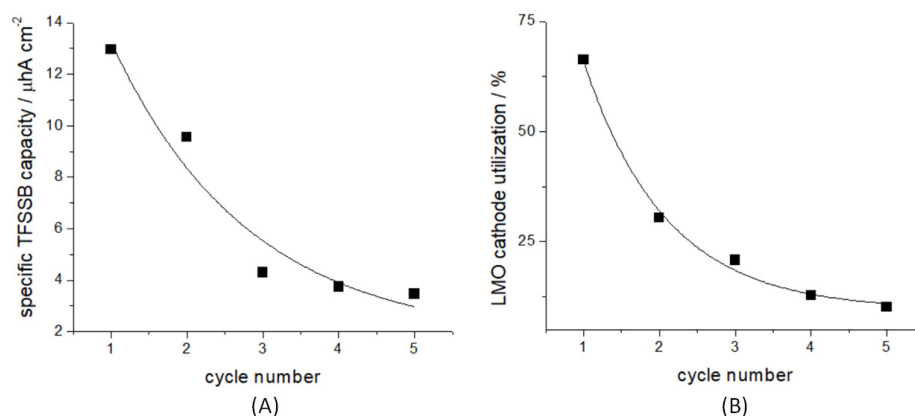
Figure 3. Electrochemical results of LMO/LAGP/Cu Li metal TFSSB ageing: (**A**) specific cell capacitance and (**B**) LMO catode utilization, as a function of the cycle number. Cycling conditions: potentiostatic intervals of 24 h at 3.0 and 4.5 V.

3.2. Chemical Mapping by Scanning Photoelectron Microscopy (SPEM)

TFSSBs were examined by SPEM in pristine state and after the application of the ageing protocol described in Section 3.1. The energies selected for imaging were centred at the Ge 3d, Al 2p, and Li 1s core levels. SPEM imaging was complemented by Visible Light Microscopy (VLM) observations. Imaging and spectro-imaging results for the pristine and aged cell are reported in Figures 4 and 5, respectively. Here we would like to stress that since this complex system may also undergo radiation damage due to charging, reduction, and dissociation [72] we show only specro-imaging results where the spectra are extracted from the images within the energy window of 4 eV. Indeed, the resolution of the spectroimaging is low, but the microspot spectra that require longer measurement times showed much stronger radiation damage effects. For these reasons, leading to a relatively poor signal-to-noise ratio, we shall refrain from fitting the micro-spectra.
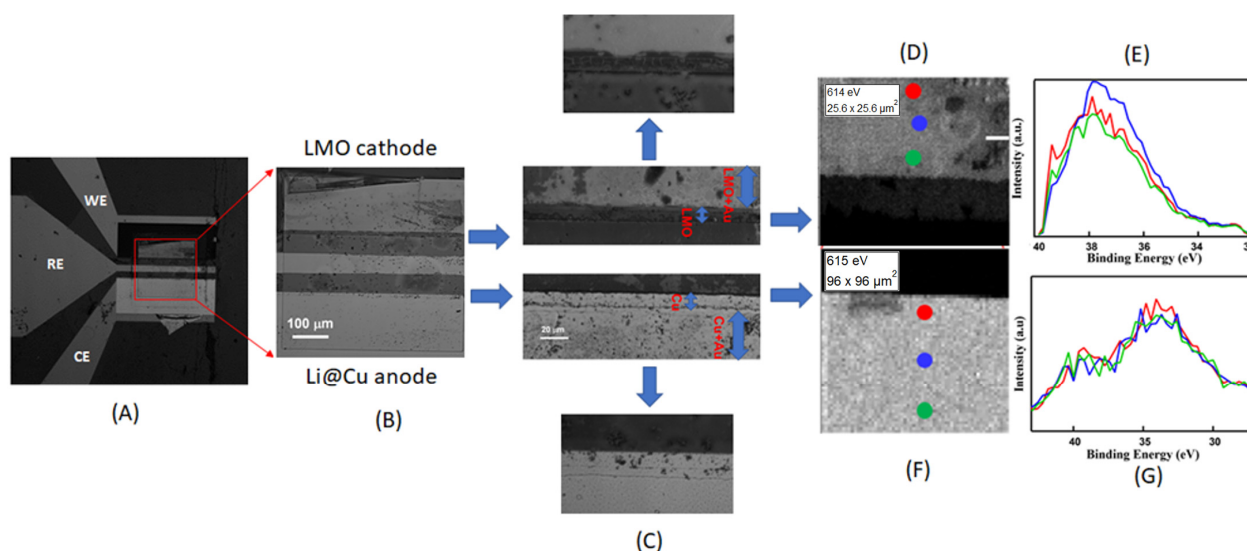

Figure 4. SPEM results for the pristine LMO/LAGP/Cu Li metal TFSSB. (**A**,**B**) VLM image of the whole cell. (**C**) VLM images of the cathode/electrolyte (**top** image) and anode/electrolyte (**bottom** image) interfacial regions. (**D**,**F**) SPEM maps at the Ge 3d core level energy of the cathode/electrolyte (**top** image) and anode/electrolyte (**bottom** image) interfacial regions. (**E**,**G**). Micro-XPS Ge 3d spectra extracted from the indicated positions of the SPEM images of Panels (**D**,**F**).

Visible Light Microscopy (VLM) (Figure 4A–C) and SPEM (Figure 4D,F) images of the electrode/electrolyte interfaces of the pristine cell were found to be homogeneous. After

cycling, appreciable morphological changes were observed at both electrodic interfaces (Figure 5A–E). Specifically, void formation was evidenced at the cathodic LMO/LAGP interface (VLM: upper image of Figure 5B; SPEM: Figure 5C) due to mechanical damage caused by the periodic volume changes accompanying the LMO delithiation–lithiation cycles. Instead, clear material accumulation features were observed at the anodic Cu/LAGP interface after charge–discharge cycles (VLM: lower image of Figure 5B; SPEM: Figure 5E), corresponding to the periodic, irreversible Li plating and stripping. These imaging results are coherent with the SEM observations of the anode of a Cu/LiPON/LCO TFSSB reported by Ref. [44], that have been explained with the growth of Li_2O crystallites, resulting from the electrolyte decomposition accompanying Li plating. In turn, the LAGP reaction correlates to the loss of active lithium inventory, capacity fade, and anode passivation.
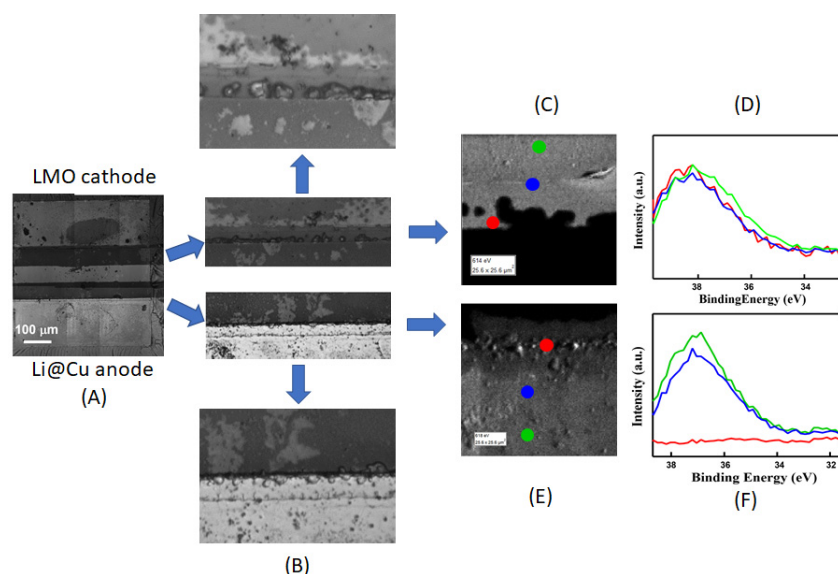

Figure 5. SPEM results for the electrochemically aged LMO/LAGP/Cu Li metal TFSSB. (**A**) VLM image of the whole cell. (**B**) VLM images of the cathode/electrolyte (**top** image) and anode/electrolyte (**bottom** image) interfacial regions. (**C,E**) SPEM maps at the Ge 3d core level energy of the cathode/electrolyte (**top** image) and anode/electrolyte (**bottom** image) interfacial regions. (**D,F**). Micro-XPS Ge 3d spectra extracted from the indicated positions of the SPEM images of Panels (**C,E**).

SPEM measurements enable a chemical-state analysis of the different regions of the cell with submicrometer space-resolution, which has not been attempted so far. They can usefully complement and deepen the few published XPS-based studies, disclosing the reductive degradation of LAGP in contact with metallic Li. In the literature, it was reported that metallic Ge and Ge-Li alloys tend to form as a result of evaporating Li onto bulk LAGP [12] or contacting LAGP with liquid Li [13]. Moreover, for the case of LATGP, Ref. [12] pinpointed a similar type of damaging, due to reduction of both Ge and Ti and alloy formation with Li. It is worth noting that, on the basis of electrochemical data, but in the absence of XPS evidence regarding the Li attack, Ref. [25] reported that sputter-coating LAGP with a thin layer of Ge would lead to the formation of a Li-Ge buffer layer, further suppressing Ge^{4+} reduction. Cognate XPS results also showed that Li sputtering onto LLTO perovskite brought about the formation of Ti^{3+} and Ti^0 from Ti^{4+} [15]. Similarly, Ge reduction upon Li^+ insertion in $NbGeO_5$ anodes was documented by Ge K-edge spectroscopy [73]. It is worth noting, in passing, that Ti^{4+} reactivity towards molten Li seems much lower in garnet-type LLZO than in phosphate-based LATGP [74], while Li sputtering onto Nb- and Ta-doped LLZO was reported to lead to the formation of Nb^{3+} and Nb^{4+} from Nb^{5+} and Zr^{2+} from Zr^{4+}, while the chemical state of Ta is stable [75].

Figure 4E,G report Ge 3d spectra, extracted from SPEM maps, of both electrodes in the pristine state. Coherently with the VLM images of Figure 4B,C, the very limited variation

of contrast is due only to fabrication-induced surface topology features, whereas the local spectra demonstrate the homogeneity of the Ge chemical state. The chemical state in the cathode region corresponds to the nominal Ge^{4+} of LAGP at the cathode [57]. Instead, a homogeneously distributed chemical-state change, corresponding to the reduction to elemental Ge [13,76] can be observed at the anode patch. This space-independent chemical state change, which does not correlate with the position within the anodic region, can be explained with beam-induced reduction, caused by local sample charging and reduction. This occurs because the cell is grounded through the cathode and the pristine LAGP layer is electronically insulating. This beam-damage phenomenon, which has not been pinpointed in the previous literature reports on LAGP, suggests special care in photoelectron measurements and mandates accurate control of possible charge accumulation at the sample surface and beam induced reduction.

The Ge 3d maps and spectra measured in both electrodic patches of the cycled cell are reported in Figure 5C–F and also in Figure 6 for comparison with pristine state, while the Al 2p and Li 1s maps and the spectra are depicted in Figure 7. These SPEM images in Figures 5 and 7 confirm the morphological changes of both the cathode and anode observed by VLM. The spectra extracted from different locations of LMO electrode (Figure 5D, and green plot of Figure 6) show that—within the limits of the available signal-to-noise ratio—the Ge chemical state remains homogeneous and identical to that of the pristine cell, denoting that void formation at the cathode/electrolyte interface is not accompanied by Ge^{4+} reactivity. On the contrary, in the anode region (Figure 5F, and purple plot of Figure 6), morphological and chemical-state changes correlate, disclosing that Ge^{4+} undergoes reduction at the cycled anode/electrolyte interface, coherently with the space-averaged results of Refs. [12,13,76], which were obtained in the absence of electrochemical control. Different positions in the interfacial region show different levels of Ge^{4+} reduction that may also be beam assisted. In the zone where morphological transformation is observed, closer to the electrolyte (the red point of Figure 5E), the Ge signal disappears. This weaker Ge 3d signal is coherent with the build-up of Li_2O at the anode/electrolyte interface conjectured by Ref. [77] and is confirmed by the fact that the Li 1s signal (Figure 7D) can be recorded only in this region. This Li accumulation phenomenon is coherent with the irreversible formation of Li oxides during the discharge periods. Instead, in internal regions that are farther from the LAGP patch (the blue and green points of Figure 5E), the dominating chemical state corresponds to Ge^{3+}, possibly due to $LiGeO_2$ formation: the presence of this species has been reported to result from the oxidation of Ge-Si alloys [78]. Moreover, at the reactive anode/LAGP interface, the Al 2p spectrum is also modified and shows an additional peak that can be assigned to Al_2O_3 [79], again resulting from LAGP decomposition. The aged cell does not show strong evidence of beam damaging: this result militates in favour of the development of MEIC in the LAGP layers damaged under battery operating conditions [1,15,20–22].
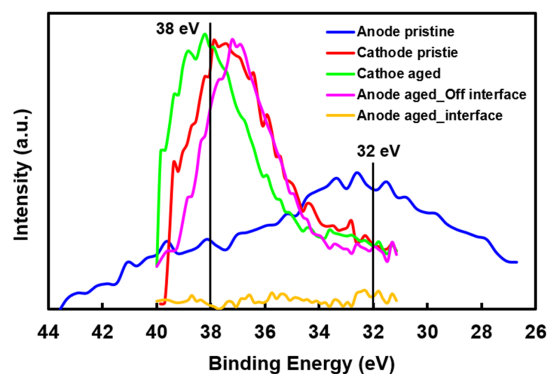

Figure 6. Overview of normalized micro-XPS Ge 3d spectra extracted from characteristic positions of the SPEM images of the cathode/electrolyte and anode/electrolyte interfacial regions depicted in Figures 4D,F and 5C,E.
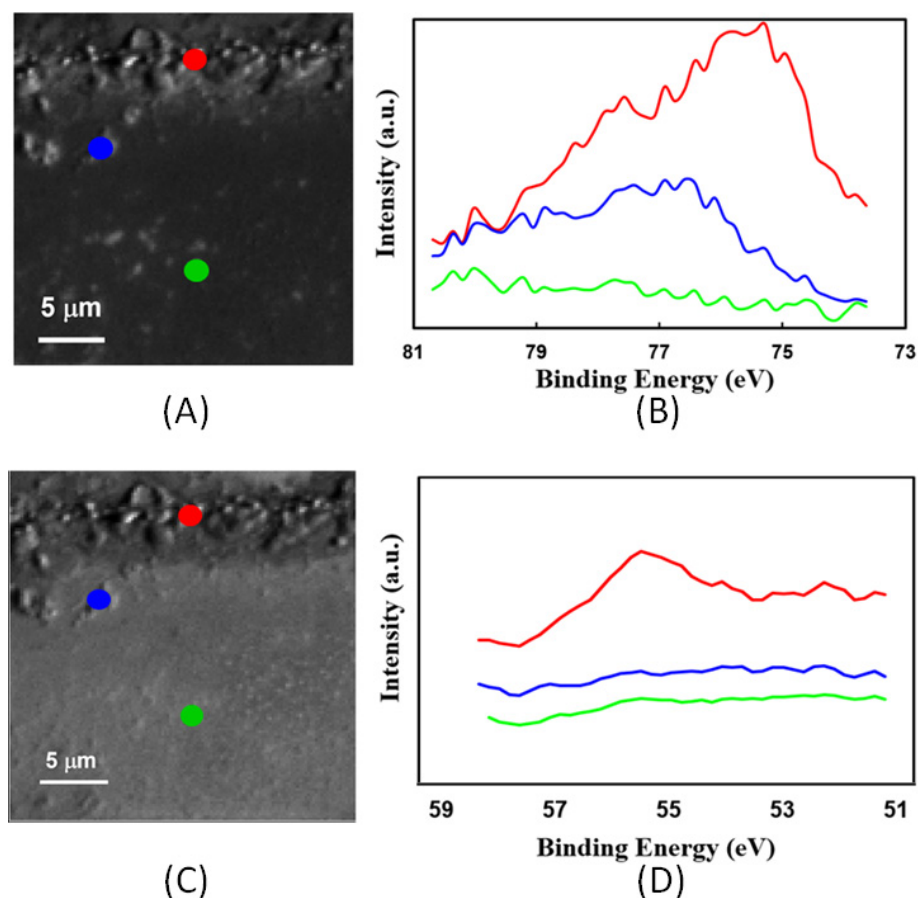
Figure 7. SPEM results for the electrochemically aged LMO/LAGP/Cu Li metal TFSSB. (**A**,**C**) SPEM maps at the Al 2p and Li 1s core level energies of the anode/electrolyte interfacial regions. (**B**,**D**) Micro-XPS Al 2p and Li 1s spectra extracted from the indicated positions of the SPEM images of Panels (**A**,**C**).

4. Conclusions

This Scanning Photoelectron Microscopy (SPEM) study of a full, intact LMO/LAGP/Cu Li metal TFSSB, pinpointed the morphochemical changes of the LAGP solid-state electrolyte, caused by formation and charge/discharge cycling. Specifically, SPEM mapping at the Ge 3d core-level revealed that the morphological changes occurring at the LMO/LAGP interface are mainly due to mechanical damaging and are not accompanied by any modification of the original Ge^{4+} chemical state. Instead, after charge/discharge cycles, the Cu/LAGP interface presents a rich scenario of Ge^{4+} reduction to Ge^0 closer to the electrode/electrolyte contact and to Ge^{3+} farther from it: both processes are triggered by the plating/stripping of Li. LAGP decomposition is further confirmed by the change in the Al 2p spectrum, compatible with the formation of Al oxide. Moreover, this chemical process is coupled with a phase-formation one, bringing about shape changes due to irreversible accumulation of the new material: possibly Li_2O and Li^+-containing LAGP degradation products, confirmed by spectroscopy at the Li 1s core level. The morphological, structural, and chemical modifications of the TFSSB brought about by electrochemical ageing, as observed in this study, are summarized in Figure 8. Reductive LAGP damaging is known from the literature, based on LAGP chemical lithiation experiments without space resolution. Our SPEM study of a complete battery, thanks to its submicrometer space resolution capability, proves for the first time that this reductive damaging mechanism is localized at the Li/LAGP interface. Moreover, we have shown that LAGP decomposition gives rise to a space distribution of degradation products, which affects the shape of the anodic solid/solid contact and its ionic and electronic conduction properties.
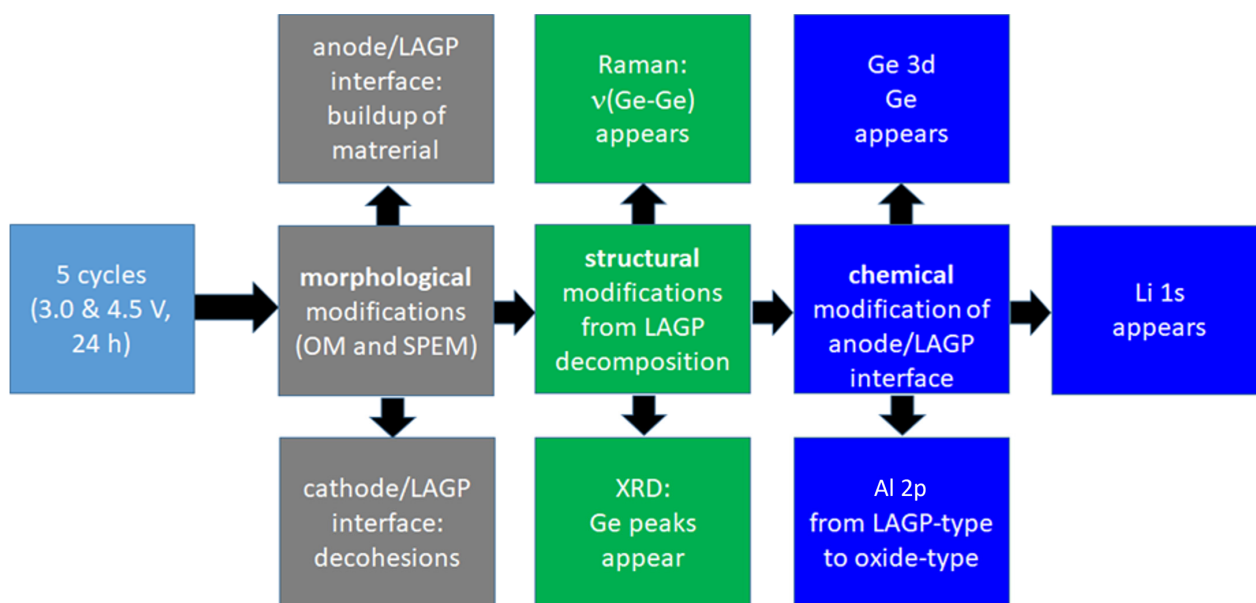
Figure 8. Scheme of the changes of LMO/LAGP/Cu Li-metal TFSSB brought about by cycling (potentiostatic intervals of 24 h at 3.0 and 4.5 V) and monitored with the SPEM-centered analytics employed in this work.

This demonstration work, dedicated to time-lapse in situ photoelectron measurements, on the one hand, proposes a route to micro-fabricate batteries, that are compatible with SPEM technical constraints, and, on the other hand, defines an experimental protocol to carry out successful photoelectron spectroscopy mapping of all functionally relevant surfaces and interfaces. The knowledge-base developed in this study, including a detailed understanding of the instrument response, also considering ways to detect and avoid beam damage, opens up the possibility of carrying out systematically dynamic in operando SPEM and micro-XPS experiments with TFSSBs.

Author Contributions: Conceptualization, M.K. (Majid Kazemian) and B.B.; methodology, M.K. (Majid Kazemian) and B.B.; software, M.K. (Majid Kazemian); validation, M.K. (Majid Kazemian), B.B. and M.K. (Maya Kiskinova); formal analysis, M.K. (Majid Kazemian) and B.B.; investigation, M.K. (Majid Kazemian) and B.B.; resources, M.K. (Majid Kazemian) and B.B. data curation, M.K. (Majid Kazemian), M.A., L.G. and B.B.; writing—original draft preparation, M.K. (Majid Kazemian) and B.B.; writing—review and editing, M.K. (Majid Kazemian), B.B., M.K. (Maya Kiskinova), M.A. and L.G.; visualization, B.B. and M.K. (Majid Kazemian); supervision, B.B.; funding acquisition, B.B. All authors have read and agreed to the published version of the manuscript.

Data Availability Statement: Data available on request. The data presented in this study are available on request from the corresponding author.

Conflicts of Interest: The authors declare no conflict of interest.

References

1. Monroe, C.; Newman, J. The Impact of Elastic Deformation on Deposition Kinetics at Lithium/Polymer Interfaces. *J. Electrochem. Soc.* **2005**, *152*, A396–A404. [CrossRef]
2. Moitzheim, S.; Put, B.; Vereecken, P.M. Advances in 3D Thin-Film Li-Ion Batteries. *Adv. Mater. Interfaces* **2019**, *6*, 1900805. [CrossRef]

3.　Li, C.; Wang, Z.-Y.; He, Z.-J.; Li, Y.-J.; Mao, J.; Dai, K.-H.; Yan, C.; Zheng, J.-C. An advance review of solid-state battery: Challenges, progress and prospects Sust. *Mater. Technol.* **2021**, *29*, e00297. [CrossRef]

4.　Chen, R.; Li, Q.; Yu, X.; Chen, L.; Li, H. Approaching Practically Accessible Solid-State Batteries: Stability Issues Related to Solid Electrolytes and Interfaces. *Chem. Rev.* **2020**, *120*, 6820–6877. [CrossRef] [PubMed]

5.　Zhao, Q.; Stalin, S.; Zhao, C.-Z.; Archer, L.A. Designing solid-state electrolytes for safe, energy-dense batteries. *Nat. Rev. Mater.* **2020**, *5*, 229–252. [CrossRef]

6.　Sun, Z.; Liu, L.; Yang, B.; Li, Q.; Wu, B.; Zhao, J.; Ma, L.; Liu, Y.; An, H. Preparation and ion conduction of $Li_{1.5}Al_{0.5}Ge_{1.5}(PO_4)_3$ solid electrolyte films using radio frequency sputtering. *Solid State Ion.* **2020**, *346*, 115224. [CrossRef]

7.　DeWees, R.; Wang, H. Synthesis and Properties of NaSICON-type LATP and LAGP Solid Electrolytes. *ChemSusChem* **2019**, *12*, 3713–3725. [CrossRef]

8.　Meesala, Y.; Chen, C.; Jena, A.; Liao, Y.; Hu, F. All-Solid-State Li-Ion Battery Using $Li_{1.5}Al_{0.5}Ge_{1.5}(PO_4)_3$ As Electrolyte Without Polymer Interfacial Adhesion. *J. Phys. Chem. C* **2018**, *122*, 14383–14389. [CrossRef]

9.　Giarola, M.; Sanson, A.; Tietz, F.; Pristat, S.; Dashjav, E.; Rettenwander, D.; Redhammer, G.J.; Mariotto, G. Structure and Vibrational Dynamics of Nasicon-Type $LiTi_2(PO_4)_3$. *J. Phys. Chem. C* **2017**, *121*, 3697–3706. [CrossRef]

10.　Xiong, L.; Ren, Z.; Xu, Y.; Mao, S.; Lei, P.; Sun, M. LiF Assisted Synthesis of $LiTi_2(PO_4)_3$ Solid Electrolyte with Enhanced Ionic Conductivity. *Solid State Ion.* **2017**, *309*, 22–26. [CrossRef]

11.　Fu, J. Fast Li+ Ion Conducting Glass-Ceramics in the System $Li_2O–Al_2O_3–GeO_2–P_2O_5$. *Solid State Ion.* **1997**, *104*, 191–194. [CrossRef]

12.　Hartmann, P.; Leichtweiss, T.; Busche, M.R.; Schneider, M.; Reich, M.; Sann, J.; Adelhelm, P.; Janek, J. Degradation of NASICON-Type Materials in Contact with Lithium Metal: Formation of Mixed Conducting Interphases (MCI) on Solid Electrolytes. *J. Phys. Chem. C* **2013**, *117*, 21064–21074. [CrossRef]

13.　He, L.; Sun, Q.; Chen, C.; Oh, J.A.S.; Sun, J.; Li, M.; Tu, W.; Zhou, H.; Zeng, K.; Lu, L. Failure Mechanism and Interface Engineering for NASICON Structured All-Solid-State Lithium Metal Batteries. *ACS Appl. Mater. Interfaces* **2019**, *11*, 20895–20904. [CrossRef] [PubMed]

14.　Feng, J.K.; Lu, L.; Lai, M.O. Lithium Storage Capability of Lithium Ion Conductor $Li_{1.5}Al_{0.5}Ge_{1.5}(PO_4)_3$. *J. Alloys Compd.* **2010**, *501*, 255–258. [CrossRef]

15.　Wenzel, S.; Leichtweiss, T.; Kruger, D.; Sann, J.; Janek, J. Interphase Formation on Lithium Solid Electrolytes-an in Situ Approach to Study Interfacial Reactions by Photoelectron Spectroscopy. *Solid State Ion.* **2015**, *278*, 98–105. [CrossRef]

16.　Robinson, J.P.; Kichambare, P.D.; Deiner, J.L.; Miller, R.; Rottmayer, M.A.; Koenig, G.M. High Temperature Electrode-Electrolyte Interface Formation between $LiMn_{1.5}Ni_{0.5}O_4$ and $Li_{1.4}Al_{0.4}Ge_{1.6}(PO_4)_3$. *J. Am. Ceram. Soc.* **2018**, *101*, 1087–1094. [CrossRef]

17.　Gellert, M.; Dashjav, E.; Gruner, D.; Ma, Q.L.; Tietz, F. Compatibility Study of Oxide and Olivine Cathode Materials with Lithium Aluminum Titanium Phosphate. *Ionics* **2018**, *24*, 1001–1006. [CrossRef]

18.　Mukhopadhyay, A.; Sheldon, B.W. Deformation and Stress in Electrode Materials for Li-Ion Batteries. *Prog. Mater. Sci.* **2014**, *63*, 58–116. [CrossRef]

19.　McGrogan, F.P.; Swamy, T.; Bishop, S.R.; Eggleton, E.; Porz, L.; Chen, X.; Chiang, Y.-M.; Van Vliet, K.J. Compliant yet Brittle Mechanical Behavior of $Li_2S–P_2S_5$ Lithium-Ion-Conducting Solid Electrolyte. *Adv. Energy Mater.* **2017**, *7*, 1602011. [CrossRef]

20.　Porz, L.; Swamy, T.; Sheldon, B.W.; Rettenwander, D.; Froemling, T.; Thaman, H.L.; Berendts, S.; Uecker, R.; Carter, W.C.; Chiang, Y.-M. Mechanism of Lithium Metal Penetration through Inorganic Solid Electrolytes. *Adv. Energy Mater.* **2017**, *7*, 1701003. [CrossRef]

21.　Swamy, T.; Park, R.; Sheldon, B.W.; Rettenwander, D.; Porz, L.; Berendts, S.; Uecker, R.; Carter, W.C.; Chiang, Y.-M. Lithium Metal Penetration Induced by Electrodeposition through Solid Electrolytes: Example in Single-Crystal $Li_6La_3ZrTaO_{12}$ Garnet. *J. Electrochem. Soc.* **2018**, *165*, A3648. [CrossRef]

22.　Han, F.; Westover, A.S.; Yue, J.; Fan, X.; Wang, F.; Chi, M.; Leonard, D.N.; Dudney, N.J.; Wang, H.; Wang, C. High Electronic Conductivity as the Origin of Lithium Dendrite Formation within Solid Electrolytes. *Nat. Energy* **2019**, *4*, 187–196. [CrossRef]

23.　Krauskopf, T.; Dippel, R.; Hartmann, H.; Peppler, K.; Mogwitz, B.; Richter, F.H.; Zeier, W.G.; Janek, J. Lithium-Metal Growth Kinetics on LLZO Garnet-Type Solid Electrolytes. *Joule* **2019**, *3*, 2030–2049. [CrossRef]

24.　Chung, H.; Kang, B. Mechanical and Thermal Failure Induced by Contact between $Li_{1.5}Al_{0.5}Ge_{1.5}(PO_4)_3$ Solid Electrolyte and Li Metal in an All Solid-State Li Cell. *Chem. Mater.* **2017**, *29*, 8611–8619. [CrossRef]

25.　Liu, Y.J.; Li, C.; Li, B.J.; Song, H.C.; Cheng, Z.; Chen, M.R.; He, P.; Zhou, H.S. Germanium Thin Film Protected Lithium Aluminum Germanium Phosphate for Solid-State Li Batteries. *Adv. Energy Mater.* **2018**, *8*, 1702374. [CrossRef]

26.　Liu, Y.L.; Sun, Q.; Zhao, Y.; Wang, B.Q.; Kaghazchi, P.; Adair, K.R.; Li, R.Y.; Zhang, C.; Liu, J.R.; Kuo, L.Y.; et al. Stabilizing the Interface of NASICON Solid Electrolyte against Li Metal with Atomic Layer Deposition. *ACS Appl. Mater. Interfaces* **2018**, *10*, 31240. [CrossRef]

27.　Li, Y.; Zhou, W.; Chen, X.; Lu, X.; Cui, Z.; Xin, S.; Xue, L.; Jia, Q.; Goodenough, J.B. Mastering the Interface for Advanced All-Solid-State Lithium Rechargeable Batteries. *Proc. Natl. Acad. Sci. USA* **2016**, *113*, 13313–13317. [CrossRef]

28.　Hao, X.G.; Zhao, Q.; Su, S.M.; Zhang, S.Q.; Ma, J.B.; Shen, L.; Yu, Q.P.; Zhao, L.; Liu, Y.; Kang, F.Y.; et al. Constructing Multifunctional Interphase between $Li_{1.4}Al_{0.4}Ti_{1.6}(PO_4)_3$ and Li Metal by Magnetron Sputtering for Highly Stable Solid-State Lithium Metal Batteries. *Adv. Energy Mater.* **2019**, *9*, 1901604. [CrossRef]

29. Hou, G.M.; Ma, X.X.; Sun, Q.D.; Ai, Q.; Xu, X.Y.; Li, D.P.; Chen, J.H.; Zhong, H.; Li, Y.; Feng, J.; et al. Lithium Dendrite Suppression and Enhanced Interfacial Compatibility Enabled by an Ex Situ SEI on Li Anode for LAGP-Based All-Solid-State Batteries. *ACS Appl. Mater. Interfaces* **2018**, *10*, 18610. [CrossRef]

30. Wenzel, S.; Randau, S.; Leichtweiss, T.; Weber, D.A.; Sann, J.; Zeier, W.G.; Janek, J. Direct Observation of the Interfacial Instability of the Fast Ionic Conductor $Li_{10}GeP_2S_{12}$ at the Lithium Metal Anode. *Chem. Mater.* **2016**, *28*, 2400–2407. [CrossRef]

31. Schwobel, A.; Hausbrand, R.; Jaegermann, W. Interface Reactions between LiPON and Lithium Studied by In-Situ X-ray Photoemission. *Solid State Ion.* **2015**, *273*, 51–54. [CrossRef]

32. Wenzel, S.; Weber, D.A.; Leichtweiss, T.; Busche, M.R.; Sann, J.; Janek, J. Interphase Formation and Degradation of Charge Transfer Kinetics between a Lithium Metal Anode and Highly Crystalline $Li_7P_3S_{11}$ Solid Electrolyte. *Solid State Ion.* **2016**, *286*, 24–33. [CrossRef]

33. Wood, K.N.; Steirer, K.X.; Hafner, S.E.; Ban, C.M.; Santhanagopalan, S.; Lee, S.H.; Teeter, G. Operando X-ray Photoelectron Spectroscopy of Solid Electrolyte Interphase Formation and Evolution in Li_2S-P_2S_5 Solid-State Electrolytes. *Nat. Commun.* **2018**, *9*, 2490. [CrossRef] [PubMed]

34. Auvergniot, J.; Cassel, A.; Ledeuil, J.; Viallet, V.; Seznec, V.; Dedryvère, R. Interface Stability of Argyrodite Li_6PS_5Cl toward $LiCoO_2$, $LiNi_{1/3}Co_{1/3}Mn_{1/3}O_2$, and $LiMn_2O_4$ in Bulk All-Solid-State Batteries. *Chem. Mater.* **2017**, *29*, 3883–3890. [CrossRef]

35. Wang, C.; Gong, Y.; Dai, J.; Zhang, L.; Xie, H.; Pastel, G.; Liu, B.; Wachsman, E.; Wang, H.; Hu, L. In Situ Neutron Depth Profiling of Lithium Metal-Garnet Interfaces for Solid State Batteries. *J. Am. Chem. Soc.* **2017**, *139*, 14257–14264. [CrossRef]

36. Yamamoto, K.; Iriyama, Y.; Asaka, T.; Hirayama, T.; Fujita, H.; Nonaka, K.; Miyahara, K.; Sugita, Y.; OgumiZ, Z. Direct Observation of Lithium-Ion Movement around an In-situ-Formed-Negative-Electrode/Solid-State-Electrolyte Interface during Initial Charge–Discharge Reaction. *Electrochem. Commun.* **2012**, *20*, 113–116. [CrossRef]

37. Yamamoto, K.; Iriyama, Y.; Asaka, T.; Hirayama, T.; Fujita, H.; Fisher, C.A.J.; Nonaka, K.; Sugita, Y.; Ogumi, Z. Dynamic Visualization of the Electric Potential in an All-Solid-State Rechargeable Lithium Battery. *Angew. Chem. Int. Ed.* **2010**, *49*, 4414–4417. [CrossRef]

38. Kazemian, M.; Kiskinova, M.; Bozzini, B. X-ray absorption spectromicroscopy gives access to LAGP local degradation at the anode-electrolyte interface. *J. Power Sources Adv.* **2022**, *17–18*, 100106. [CrossRef]

39. Zhang, T.; Imanishi, N.; Shimonishi, Y.; Hirano, A.; Takeda, Y.; Yamamoto, O.; Sammes, N. A Novel High Energy Density Rechargeable Lithium/Air Battery. *Chem. Commun.* **2010**, *46*, 1661–1663. [CrossRef]

40. Shimonishi, Y.; Zhang, T.; Imanishi, N.; Im, D.; Lee, D.J.; Hirano, A.; Takeda, Y.; Yamamoto, O.; Sammes, N. A Study on Lithium/Air Secondary Batteries-Stability of the Nasicon-Type Lithium Ion Conducting Solid Electrolyte in Alkaline Aqueous Solutions. *J. Power Sources* **2011**, *196*, 5128–5132. [CrossRef]

41. Dashjav, E.; Ma, Q.L.; Xu, Q.; Tsai, C.L.; Giarola, M.; Mariotto, G.; Tietz, F. The Influence of Water on the Electrical Conductivity of Aluminum-Substituted Lithium Titanium Phosphates. *Solid State Ion.* **2018**, *321*, 83–90. [CrossRef]

42. Benabed, Y.; Rioux, M.; Rousselot, S.; Hautier, G.; Dollé, M. Assessing the Electrochemical Stability Window of NASICON-Type Solid Electrolytes. *Front. Energy Res.* **2021**, *9*, 682008. [CrossRef]

43. Tan, G.; Wu, F.; Li, L.; Liu, Y.; Chen, R. Magnetron sputtering preparation of nitrogen-incorporated lithium–aluminum–titanium phosphate based thin film electrolytes for all-solid-state lithium ion batteries. *J. Phys. Chem. C* **2012**, *116*, 3817–3826. [CrossRef]

44. Neudecker, B.J.; Dudney, N.J.; Bates, J.B. Lithium-Free" Thin-Film Battery with In Situ Plated Li Anode. *J. Electrochem. Soc.* **2000**, *147*, 517–523. [CrossRef]

45. Qin, J.; Adams, B.D.; Zheng, J.; Xu, W.; Henderson, W.A.; Wang, J.; Bowden, M.E.; Xu, S.; Hu, J.; Zhang, J. Anode-Free Rechargeable Lithium Metal Batteries. *Adv. Funct. Mater.* **2016**, *26*, 7094–7102. [CrossRef]

46. Bates, J.B.; Dudney, N.J.; Neudecker, B.J.; Hart, F.X.; Jun, H.P.; Hackney, S.A. Preferred Orientation of Polycrystalline $LiCoO_2$ Films. *J. Electrochem. Soc.* **2000**, *147*, 59. [CrossRef]

47. Lee, K.L.; Jung, J.Y.; Lee, S.W.; Moon, H.S.; Park, J.W. Electrochemical characteristics and cycle performance of $LiMn_2O_4$/a-Si microbattery. *J. Power Sources* **2004**, *130*, 241–246. [CrossRef]

48. Otsuji, H.; Kawahara, K.; Ikegami, T.; Ebihara, K. $LiMn_2O_4$ thin films prepared by pulsed laser deposition for rechargeable batteries. *Thin Solid Film.* **2006**, *506*, 120–122. [CrossRef]

49. Liu, P.; Zhang, J.G.; Turner, J.A.; Tracy, C.E.; Benson, D.K. Lithium-Manganese-Oxide Thin-Film Cathodes Prepared by Plasma-Enhanced Chemical Vapor Deposition. *J. Electrochem. Soc.* **1999**, *146*, 2001–2005. [CrossRef]

50. Delluva, A.A.; Dudoff, J.; Teeter, G.; Holewinski, A. Cathode Interface Compatibility of Amorphous $LiMn_2O_4$ (LMO) and $Li_7La_3Zr_2O_{12}$ (LLZO) Characterized with Thin-Film Solid-State Electrochemical Cells. *ACS Appl. Mater. Interfaces* **2020**, *12*, 24992–24999. [CrossRef]

51. Bates, J.B.; Dudney, N.J.; Neudecker, B.; Ueda, A.; Evans, C.D. Thin-film lithium and lithium-ion batteries. *Solid State Ion.* **2000**, *135*, 33–45. [CrossRef]

52. Dudney, N.J. Solid-state thin-film rechargeable batteries. *Mater. Sci. Eng. B* **2005**, *116*, 245–249. [CrossRef]

53. Ren, Y.; Liu, T.; Shen, Y.; Lin, Y.; Nan, C.W. Chemical Compatibility between Garnet-like Solid State Electrolyte $Li_{6.75}La_3Zr_{1.75}Ta_{0.25}O_{12}$ and Major Commercial Lithium Battery Cathode Materials. *J. Mater.* **2016**, *2*, 256–264. [CrossRef]

54. Mousavi, T.; Chen, X.; Doerrer, C.; Jagger, B.; Speller, S.C.; Grovenor, C.R.M. Fabrication of $Li1_{+x}Al_xGe_{2-x}(PO_4)_3$ thin films by sputtering for solid. *Solid State Ion.* **2020**, *354*, 115397. [CrossRef]

55. Tian, L.; Yuan, A. Electrochemical performance of nanostructured spinel $LiMn_2O_4$ in different aqueous electrolytes. *J. Power Sources* **2009**, *192*, 693–697. [CrossRef]

56. Liu, X.; Tan, J.; Fu, J.; Yuan, R.; Wen, H.; Zhang, C. Facile Synthesis of Nanosized Lithium-Ion-Conducting Solid Electrolyte $Li_{1.4}Al_{0.4}Ti_{1.6}(PO_4)_3$ and Its Mechanical Nanocomposites with $LiMn_2O_4$ for Enhanced Cyclic Performance in Lithium Ion Batteries. *ACS Appl. Mater. Interfaces* **2017**, *9*, 11696–11703. [CrossRef]

57. Das, A.; Krishna, P.S.R.; Goswami, M.; Krishnan, M. Structural analysis of Al and Si substituted lithium germanium phosphate glass-ceramics using neutron and X-ray diffraction. *J. Solid State Chem.* **2019**, *271*, 74–80. [CrossRef]

58. Yu, Q.; Han, D.; Lu, Q.; He, Y.-B.; Li, S.; Liu, Q.; Han, C.; Kang, F.; Li, B. Constructing Effective Interfaces for $Li_{1.5}Al_{0.5}Ge_{1.5}(PO_4)_3$ Pellets To Achieve Room-Temperature Hybrid Solid-State Lithium Metal Batteries. *ACS Appl. Mater. Interfaces* **2019**, *11*, 9911–9918. [CrossRef]

59. Li, Z.; Zhang, S.; Qian, K.; Li, T.; Wei, G.; Kang, F. Efficient Construction of a C60 Interlayer for Mechanically Robust, Dendrite-free, and Ultrastable Solid-State Batteries. *iScience* **2020**, *23*, 101636. [CrossRef]

60. Lam, Y.C.; Zheng, H.Y.; Tjeung, R.T.; Chen, X. Seeing the invisible laser markings. *J. Phys. D: Appl. Phys.* **2009**, *42*, 042004. [CrossRef]

61. Yan, W.; Li, H.; Liu, J.; Guo, J. EPMA and XRD study on nickel metal thin film for temperature sensor. *Sens. Actuators A* **2007**, *136*, 212–215. [CrossRef]

62. Tarte, P.; Rulmont, A.; Merckaert-Ansay, C. Vibrational spectrum of nasicon-like, rhombohedral orthophosphates $MIMIV_2(PO_4)_3$. *Spectrochim. Acta A* **1986**, *42*, 1009–1016. [CrossRef]

63. Francisco, B.E.; Stoldt, C.R.; M'Peko, J.C. Lithium-Ion Trapping from Local Structural Distortions in Sodium Super Ionic Conductor (NASICON) Electrolytes. *Chem. Mater.* **2014**, *26*, 4741–4749. [CrossRef]

64. Pershina, S.V.; Pankratov, A.A.; Vovkotrub, E.G.; Antonov, B.D. Promising high-conductivity $Li_{1.5}Al_{0.5}Ge_{1.5}(PO_4)_3$ solid electrolytes: The effect of crystallization temperature on the microstructure and transport properties. *Ionics* **2019**, *25*, 4713–4725. [CrossRef]

65. Abyaneh, M.K.; Gregoratti, L.; Amati, M.; Dalmiglio, M.; Kiskinova, M. Scanning photoelectron microscopy: A powerful technique for probing micro and nano-structures. *J. Surf. Sci. Nanotechnol.* **2011**, *9*, 158–162. [CrossRef]

66. Dudney, N.J. Evolution of the lithium morphology from cycling of thin film solid state batteries. *J. Electroceramics* **2017**, *38*, 222–229. [CrossRef]

67. Guo, X.; Hao, L.; Yang, Y.; Wang, Y.; Yu, Y.L.H. High cathode utilization efficiency through interface engineering in all-solid state lithium-metal batteries. *J. Mater. Chem. A* **2019**, *7*, 25915–25924. [CrossRef]

68. Sorianello, V.; Colace, L.; Armani, N.; Rossi, F.; Ferrari, C.; Lazzarini, L.; Assanto, G. Low-temperature germanium thin films on silicon. *Opt. Mater. Express* **2011**, *1*, 856–865. [CrossRef]

69. Parker, J.H., Jr.; Feldman, D.W.; Ashkin, M. Raman scattering by Silicon and Germanium. *Phys. Rev.* **1967**, *155*, 712. [CrossRef]

70. D'Costa, V.R.; Tolle, J.; Poweleit, C.D.; Kouvetakis, J. Compositional dependence of the Raman frequencies in ternary Ge1-x-ySixSny alloys. *Phys. Rev. B* **2007**, *76*, 035211. [CrossRef]

71. Zanatta, A.R. Temperature-dependent Raman scattering of the Ge+GeOx system and its potential as an optical thermometer. *Results Phys.* **2020**, *19*, 103500. [CrossRef]

72. Gregoratti, L.; Mentes, T.O.; Locatelli, A.; Kiskinova, M. Beam-induced effects in soft X-ray photoelectron emission microscopy experiments. *J. Electron Spectrosc. Relat. Phenom.* **2009**, *170*, 13–18. [CrossRef]

73. Cao, X.; Cao, Y.; Peng, H.; Cao, Y.; Zhu, H.; Wang, N.; Dong, X.; Wang, C.; Liu, Y.; Wu, J.; et al. A New Germanium-Based Anode Material with High Stability for Lithium-Ion Batteries. *ACS Sustain. Chem. Eng.* **2021**, *9*, 11883–11890. [CrossRef]

74. Wolfenstine, J.; Allen, J.L.; Read, J.; Sakamoto, J. Chemical Stability of Cubic $Li_7La_3Zr_2O_{12}$ with Molten Lithium at Elevated Temperature. *J. Mater. Sci.* **2013**, *48*, 5846–5851. [CrossRef]

75. Zhu, Y.; Connell, J.G.; Tepavcevic, S.; Zapol, P.; Garcia-Mendez, R.; Taylor, N.J.; Sakamoto, J.; Ingram, B.J.; Curtiss, L.A.; Freeland, J.W.; et al. Dopant-Dependent Stability of Garnet Solid Electrolyte Interfaces with Lithium Metal. *Adv. Energy Mater.* **2019**, *9*, 1803440. [CrossRef]

76. Wang, L.; Liu, D.; Huang, T.; Geng, Z.; Yu, A. Reducing interfacial resistance of a $Li_{1.5}Al_{0.5}Ge_{1.5}(PO_4)_3$ solid electrolyte/electrode interface by polymer interlayer protection. *RSC Adv.* **2020**, *10*, 10038–10045. [CrossRef]

77. Etxebarria, A.; Yun, D.-J.; Blum, M.; Ye, Y.; Sun, M.; Lee, K.-J.; Su, H.; Muñoz-Márquez, M.Á.; Ross, P.N.; Crumlin, E.J. Revealing In Situ Li Metal Anode Surface Evolution upon Exposure to CO_2 Using Ambient Pressure X-ray Photoelectron Spectroscopy. *ACS Appl. Mater. Interfaces* **2020**, *12*, 26607–26613. [CrossRef]

78. Bensalah, N.; Matalkeh, M.; Mustafa, N.K.; Merabet, H. Binary Si–Ge Alloys as High-Capacity Anodes for Li-Ion Batteries. *Phys. Status Solidi A* **2020**, *217*, 1900414. [CrossRef]

79. Hoque, E.; DeRose, J.A.; Kulik, G.; Hoffmann, P.; Mathieu, H.J.; Bhishan, B. Alkylphosphonate Modified Aluminium Oxide Surfaces. *J. Phys. Chem. B* **2006**, *110*, 10855–10861. [CrossRef]